

Article

Mobilization of Au and Ag during Supergene Processes in the Linglong Gold Deposit: Evidence from SEM and LA-ICP-MS Analyses of Sulfides

Hong Wang^{1,2}, Tingguang Lan^{1,2,*}, Yinghua Chen^{1,2}, Huanlong Hu¹ and Lei Shu³

¹ State Key Laboratory of Ore Deposit Geochemistry, Institute of Geochemistry, Chinese Academy of Sciences, Guiyang 550081, China; wanghong@mail.gyig.ac.cn (H.W.); chenyinghua@mail.gyig.ac.cn (Y.C.); huhuanlong@mail.gyig.ac.cn (H.H.)

² University of Chinese Academy of Sciences, Beijing 100049, China

³ MNR Key Laboratory of Gold Mineralization Processes and Resources Utilization, Shandong Institute of Geological Sciences, Jinan 250013, China; shuleidky@shandong.cn

* Correspondence: lantingguang@126.com

Abstract: Precious metals can be mobilized during supergene processes, which are important for the formation of high-grade or high-purity ores. The world-class Linglong gold deposit has high-grade ores that have undergone supergene processes in the near-surface zone. Under which conditions the supergene modification occurred and how Au and Ag behaved during the supergene processes have been poorly studied in this deposit. Here, we performed scanning electron microscope (SEM) and laser ablation-inductively coupled plasma-mass spectrometry (LA-ICP-MS) analyses on samples from the supergene enrichment zone of the Linglong gold deposit. The results show that secondary minerals were formed sequentially from magnetite-goethite-limonite to marcasite-acanthite, and finally to siderite after the primary minerals of pyrite-pyrrhotite-chalcocopyrite. These mineral assemblages and variations indicate that the supergene modification by groundwater occurred under oxidative and weakly acidic conditions in the near-surface zone and evolved to reductive and near neutral conditions in the supergene enrichment zone. The newly formed marcasite has much higher Au (0.003–23.5 ppm, mean of 1.33 ppm) and Ag (81.7–6021 ppm, mean of 1111 ppm) concentrations than those of the primary pyrite (Au of 0.004–0.029 ppm and Ag of 0.22–4.14 ppm), which together with the formation of independent Ag–S mineral (acanthite), indicates that Au and Ag were significantly mobilized and fractionated during the supergene processes. These processes improved the Au and Ag grades in the supergene enrichment zone and thus facilitate their extraction.

Keywords: Linglong gold deposit; supergene; pyrite; marcasite; LA-ICP-MS; trace element



Citation: Wang, H.; Lan, T.; Chen, Y.; Hu, H.; Shu, L. Mobilization of Au and Ag during Supergene Processes in the Linglong Gold Deposit: Evidence from SEM and LA-ICP-MS Analyses of Sulfides. *Minerals* **2022**, *12*, 367. <https://doi.org/10.3390/min12030367>

Academic Editors: Maria Boni and Stefano Salvi

Received: 25 January 2022

Accepted: 14 March 2022

Published: 16 March 2022

Publisher's Note: MDPI stays neutral with regard to jurisdictional claims in published maps and institutional affiliations.



Copyright: © 2022 by the authors. Licensee MDPI, Basel, Switzerland. This article is an open access article distributed under the terms and conditions of the Creative Commons Attribution (CC BY) license (<https://creativecommons.org/licenses/by/4.0/>).

1. Introduction

High-grade ores are crucial in the mineral industry, as they greatly reduce the exploitation costs. Such ores in gold deposits can be generated through hypogene hydrothermal processes, such as the dissolution–reprecipitation of the primary Au-bearing minerals [1,2], the interaction between auriferous fluids and wall rocks [3], and the phase separation or boiling of the auriferous fluids [4,5]. Notably, it is found that postdepositional supergene processes can also lead to the enrichment of Au [6–10]. The term “supergene process” is used to describe the near-surface alteration and modification by descending groundwater at low temperatures and pressures [11,12]. A typical supergene profile of a gold deposit consists of (1) a leached cap, (2) an oxidized zone, (3) a supergene enrichment zone, and (4) the primary ore zone [11]. Free particles of high-purity Au (>99% Au) commonly occur in the former two zones as the result of the refinement of Au and the removal of Ag and other metals from Au–Ag alloys and sulfides [12,13]. These metals are transported downward and concentrated beneath the oxidation zone, forming the supergene enrichment

zone. These processes not only lead to the enrichment of the precious metals, but also fractionation between them. Investigating the metal behaviors during supergene processes is thus critical for understanding the postdepositional formation of high-grade or high-purity ores and is useful for exploration strategies.

The Jiaodong Peninsula is the largest gold province in China, hosting more than 5000 tons of gold resources [14]. The Linglong gold deposit, which contains more than 150 tons of gold, is one of the largest gold deposits in this region [15,16]. Some of ore veins in this deposit show remarkably high Au grades (up to hundreds of grams per ton) and have undergone supergene processes [15–18]. Under which conditions the supergene processes occurred and how precious metals behaved during these processes in the Linglong gold deposit have not been well constrained. In this contribution, we used in-situ analysis of laser ablation–inductively coupled plasma–mass spectrometry (LA–ICP–MS), combined with scanning electron microscope (SEM), to study the micro-textures and trace elemental compositions of pyrite and marcasite from the ore veins that underwent supergene modification at Linglong. This study reveals how the Au and Ag were mobilized during supergene processes and yields insights into the formation of high-grade or high-purity ores.

2. Geological Setting

2.1. Regional Geology

The Jiaodong Peninsula is located at the eastern margin of the North China Craton (NCC). It is tectonically composed of the Jiaobei terrane in the west and the Sulu ultrahigh-pressure orogen in the east (Figure 1a). The Jiaobei terrane, which mainly consists of Precambrian basement rocks and Mesozoic granitoids and volcanics [19], can be subdivided into the Jiaobei uplift in the north and the Jiaolai basin in the south. The Precambrian basement rocks include Mesoarchean to Neoproterozoic (2.9–2.7 Ga) tonalite–trondhjemitic–granodiorite gneisses, biotite–plagioclase gneisses and amphibolites, Paleoproterozoic (2.3–2.0 Ga) sillimanite–biotite–quartz schists, biotite leptytes and gneisses, amphibolites, marbles, and graphite-bearing rocks [20,21]. The Mesozoic granitoids include Late Jurassic (160–150 Ma) granites [22,23], and Early Cretaceous (130–113 Ma) granodiorites, (alkaline) granites, and monzonites [23–25]. Mafic to felsic dykes, which were emplaced at the Early Cretaceous (131–110 Ma), are also widespread in the Jiaobei terrane [26].

More than 150 gold deposits occur in Jiaodong Peninsula, most of which formed at 120 ± 2 Ma within the Jiaobei uplift [14,27,28]. The gold deposits are controlled by NE- to NNE-trending faults and are mainly hosted in the Mesozoic granitoids, with some in the Precambrian metamorphic rocks. Two mineralization types have been identified, which are called the Jiaojia type and the Linglong type, respectively [28]. The former type is characterized by disseminated and stockwork ores in the altered rocks, while the latter is characterized by auriferous quartz–sulfide veins in the fractures. The two types of mineralization are similar in formation ages, wall rocks, alteration types, and fluid inclusions [15,16,29], but can differ in structural settings, where the Linglong type mainly occurs in the lower-order, steep-dipping ($>60^\circ$) fractures distal to the regional-scale main faults, while the Jiaojia type occurs in the less steep ($<45^\circ$) fractures close to the main faults [28,30].

Supergene modification took place in the near-surface zone of some gold deposits in the Jiaodong Peninsula [17,18,31]. From the ground surface downward, the supergene zones include an oxidation zone and a supergene sulfide enrichment zone. The oxidation zone mainly contains secondary oxides with minor sulfides [17,18]. The supergene enrichment zone is composed of primary and secondary sulfides with minor oxides. Below the supergene enrichment zone is the primary ore zone. There are four hydrothermal stages in the primary ore zone [15,16]. Stage 1 mainly contains the mineral assemblage of quartz \pm pyrite without gold. Stage 2 is characterized by the assemblage of gold–quartz–pyrite. Stage 3 is characterized by the assemblage of gold–quartz–polymetallic sulfides (such as pyrite, chalcopyrite, pyrrhotite, galena, and sphalerite). Stage 4 mainly contains quartz–calcite \pm pyrite without gold.

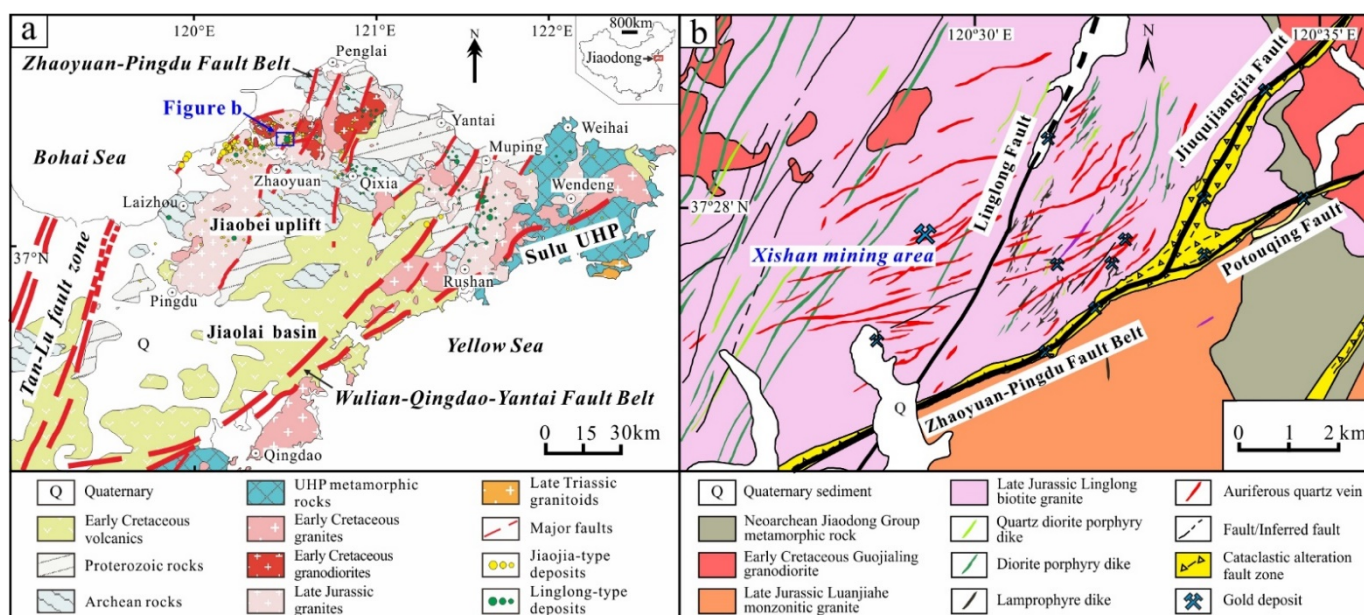


Figure 1. (a) Regional geological map of the Jiaodong Peninsula and the distribution of gold deposits (modified after [32]). **(b)** Simplified geological map of the Linglong goldfield (modified after [15]). Samples of this study were collected from the Xishan mining area.

2.2. Deposit Geology

The Linglong gold deposit consists of more than 100 steeply dipping and NE-trending quartz–sulfide veins, which occur in the secondary faults of the Zhaoyuan–Pingdu fault belt (Figure 1b) [15,16]. The ore veins are dominantly hosted in the Late Jurassic Linglong biotite granite and subordinately in the Early Cretaceous Guojialing granodiorite. The deposit contains several mining areas, of which the Xishan is a major one. The ore vein #108 at Xishan is the largest. It is about 5300 m long and 0.8 m to 6.0 m thick, striking to the northeast and dipping about 60° to the northwest. The gold grade varies widely from several to hundreds of grams per ton (mean of 15 g/t). The primary mineral assemblages of the veins are quartz and minor pyrite in stage 1; quartz and pyrite with minor chalcopyrite, galena, and sphalerite in stage 2; quartz and pyrite with abundant chalcopyrite, pyrrhotite, galena, and sphalerite in stage 3; and quartz and calcite in stage 4. Stages 2 and 3 are the ore-forming stages, in which gold mainly occurs as μm -scale grains in pyrite. Hydrothermal alterations in the wall rocks are potash feldspathization, silicification, sericitization, pyritization, and carbonatization.

The postdepositional supergene zones of ore veins occur near the surface along the fractures [17,18]. Two supergene zones, i.e., the oxidation (leached) zone and the supergene enrichment zone, were identified by previous studies (Figure 2) [17,18]. The thickness of the oxidation zone is usually 5–10 m, and up to 30 m locally. The minerals in the oxidation zone mainly include goethite, lepidocrocite, and jarosite, with minor hydrohematite, pyrolusite, malachite, and native copper. The primary sulfides have been almost completely oxidized. Only a small amount of pyrite remains locally. The oxidized minerals were formed either in situ or ex situ. The in situ-formed minerals commonly retain the textures of their primary ones, and there are residual gold grains. The ex situ-formed minerals occur as veinlets filling in the fractures and do not contain visible gold grains. Previous studies by Wang and Feng [18] showed that 90% of the samples ($n = 5427$) from the oxidation zone contain Au grades less than 0.10 g/t, and 7.5% of the samples contain Au grades between 0.10 g/t and 0.85 g/t. Only few samples contain Au grades greater than 3.0 g/t. The average leaching loss rate of Au in the oxidation zone is 89% [17,18].

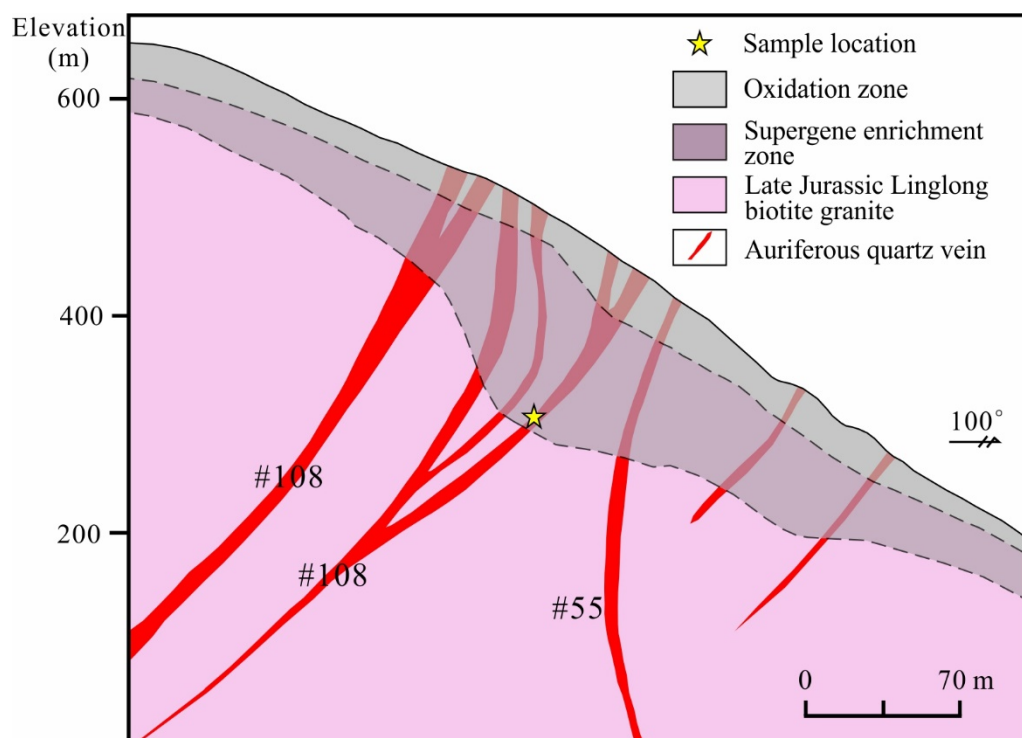


Figure 2. The geological profile along prospecting line #32 in the Xishan mining area (modified after [17]).

The supergene enrichment zone is developed below the oxidation zone. The lower boundary of the supergene enrichment zone is at the depths of 10–30 m, and up to 100 m locally. The primary sulfides in this zone are pyrite, chalcopyrite, galena, sphalerite, and pyrrhotite. The secondary minerals mainly include goethite, lepidocrocite, and hydrohematite, with minor bornite, covellite, marcasite, acanthite, and siderite. Primary pyrite and chalcopyrite are commonly replaced by marcasite and iron oxides along the edges and microfractures, thereby forming the ring, grid, and stockwork structures. The oxide content decreases with the increase in depth. Gold grains can be found in pyrite. The Au grade in this zone is 15–30 g/t, and the secondary enrichment rate of Au is 48% [17,18].

The underlying primary ore zone is composed of quartz and sulfides (such as pyrite, chalcopyrite, pyrrhotite, sphalerite, and galena). Near the top of this zone, pyrrhotite has been partially transformed into the new minerals of pyrite, colloidal pyrite, and marcasite [17]. Gold mainly occurs as visible electrum or native gold grains in the fractures of the pyrite.

3. Samples and Methods

Due to many years of open-pit and underground mining, the oxidized zone and parts of the supergene enrichment zone in the studied deposit have been excavated. Nonetheless, five samples containing primary and secondary minerals in the supergene enrichment zone were collected from the ore vein #108 in the Xishan mining area at the mining tunnels with an elevation of ~300 m. Those samples were prepared into six thin sections for petrographic observations and then for SEM and LA-ICP-MS analyses. All the analyses were conducted at the State Key Laboratory of Ore Deposit Geochemistry (SKLOGD), Institute of Geochemistry, Chinese Academy of Sciences (IGCAS), Guiyang, China.

3.1. SEM Analysis

Scanning electron microscope observations (SEM) were carried out with a JEOL JSM-7800F SEM equipped with an EDAX TEAM Apollo XL energy dispersive X-ray spectrometer (EDS) and a Gatan MonoCL4 cathodoluminescence detector. The working conditions

were a beam size of 1 μm , an accelerating voltage of 20 kV, and an incident current of 10 nA. Backscattered electron (BSE) imaging, EDS mineral identification, and EDS mapping were performed.

3.2. LA-ICP-MS Elemental Determination

Quantitative major and trace element determinations of pyrite and marcasite were conducted by LA-ICP-MS with a RESOLUTION S-155 ArF 193 nm laser ablation system (Australian Scientific Instruments, Fyshwick, ACT, Australia) coupled to an Agilent 7700 \times quadrupole ICP-MS. Helium (370 mL/min) was applied as a carrier gas. The ablated aerosols were mixed with argon (900 mL/min) via a Y-connector before entering the ICP.

Each spot analysis included a background acquisition of approximately 20 s (laser off) and data acquisition from the sample (laser on) of 60 s, and then the laser was turned off for about 40 s to eliminate the memory effects. A laser spot size of 26 μm , a repetition of 6 Hz, and a fluence of 3 J/cm² were used during the analyses. Multiple external standards were used for calibration, of which the sulfide standard STDGL2b2 was used to calibrate the concentrations of chalcophile and siderophile elements, while the glass standard GSD-1G was used to calibrate the lithophile elements. The MASS-1 and GSE-1G were also analyzed to monitor the accuracy, and show that most of the analyzed elements have accuracies better than 10%. The preferred elemental concentrations for the USGS reference glasses (GSD-1G and GSE-1G) are from the GeoReM database (http://georem.mpch-mainz.gwdg.de/sample_query_pref.asp, accessed on 24 January 2022), while the MASS-1 and STDGL2b2 are from Wilson et al. [33] and Danyushevsky et al. [34], respectively. The data processing was performed with the Iolite software [35].

3.3. LA-ICP-MS Element-Distribution Mapping

The semi-quantitative distribution of the elements was also conducted by the above LA-ICP-MS instruments. The interested areas were preselected based on detailed petrographic observations and then ablated by defining a number of equally spaced lines. The lines were ablated using a laser spot size of 22 μm , a repetition rate of 10 Hz, a fluence of 3 J/cm², and a scanning speed of 22 $\mu\text{m/s}$. After setting up the appropriate ablation parameters, the analyses were fully automated and controlled by the laser software of GeoStar and the mass spectrometer. The processing and imaging of the data were performed with the Iolite software [35]. The sulfide standard STDGL2b2 and glass standard GSD-1G were used as semi-quantitative calibration standards.

4. Results

4.1. Mineral Assemblages and Microtextures

Based on the petrographic and SEM observations, the studied samples are dominantly composed of pyrite, quartz, chalcopyrite, siderite, pyrrhotite, and marcasite, with sub-ordinary magnetite and goethite/limonite and minor sphalerite, galena, acanthite, and visible gold grains (Figures 3 and 4). Pyrite, pyrrhotite, and chalcopyrite are the main primary sulfides, which are replaced by marcasite, magnetite, siderite, goethite, and limonite along their fractures, margins, or surfaces (Figure 3c–i). Pyrrhotite is also replaced by secondary pyrite along fractures or surfaces (Figure 3g,h). The primary partially pyrite grains are coarse-grained with subhedral to anhedral shapes (Figures 3c–f,i and 5a), which commonly show mosaic or homogeneous textures under BSE imaging (Figure 5b,d). A small amount of secondary pyrite only occurs in the fractures within pyrrhotite. Sphalerite and galena are fine-grained and mainly occur as inclusions within pyrite or chalcopyrite (Figures 4g,h and 5d). Magnetite and limonite are coexistent and secondary, which seem to be converted from pyrrhotite (Figure 3g,h). The secondary goethite ribs are elongate with sizes of <10 microns, occurring along the surfaces of the pyrite grains (Figure 3i). Marcasite is the main secondary sulfide, showing tabular shape and polysynthetically twinning texture (Figure 3e,f). Siderite commonly fills in the fractures of sulfides (Figure 3e,g) or replaces chalcopyrite (Figure 4f,g). Both primary and secondary quartz occur, of which the

former coexists with pyrite and is well crystallized (megacrystalline) with a white color (Figure 3a). The latter is cryptocrystalline or colloidal, cementing secondary siderite and sulfides (Figure 3b). Gold grains can be identified in the fractures of pyrite (Figure 4a–c) or as inclusions in the pyrite (Figures 3e and 4d,e) and quartz (Figure 4f). They have irregular shapes and range from several to 100 microns in size. There was no visible gold grain found in the secondary minerals such as marcasite, siderite, and oxides. Acanthite grains can be found along the surfaces of chalcopyrite and commonly coexist with siderite (Figures 3d, 4g–i and 5d). They are irregular with variable sizes (several to 200 microns) and contain voids and mineral inclusions in the core (Figure 5d). In general, secondary minerals were formed sequentially from magnetite-goethite-limonite to marcasite-acanthite, and finally to siderite after the primary minerals of pyrite-pyrrhotite-chalcopyrite.

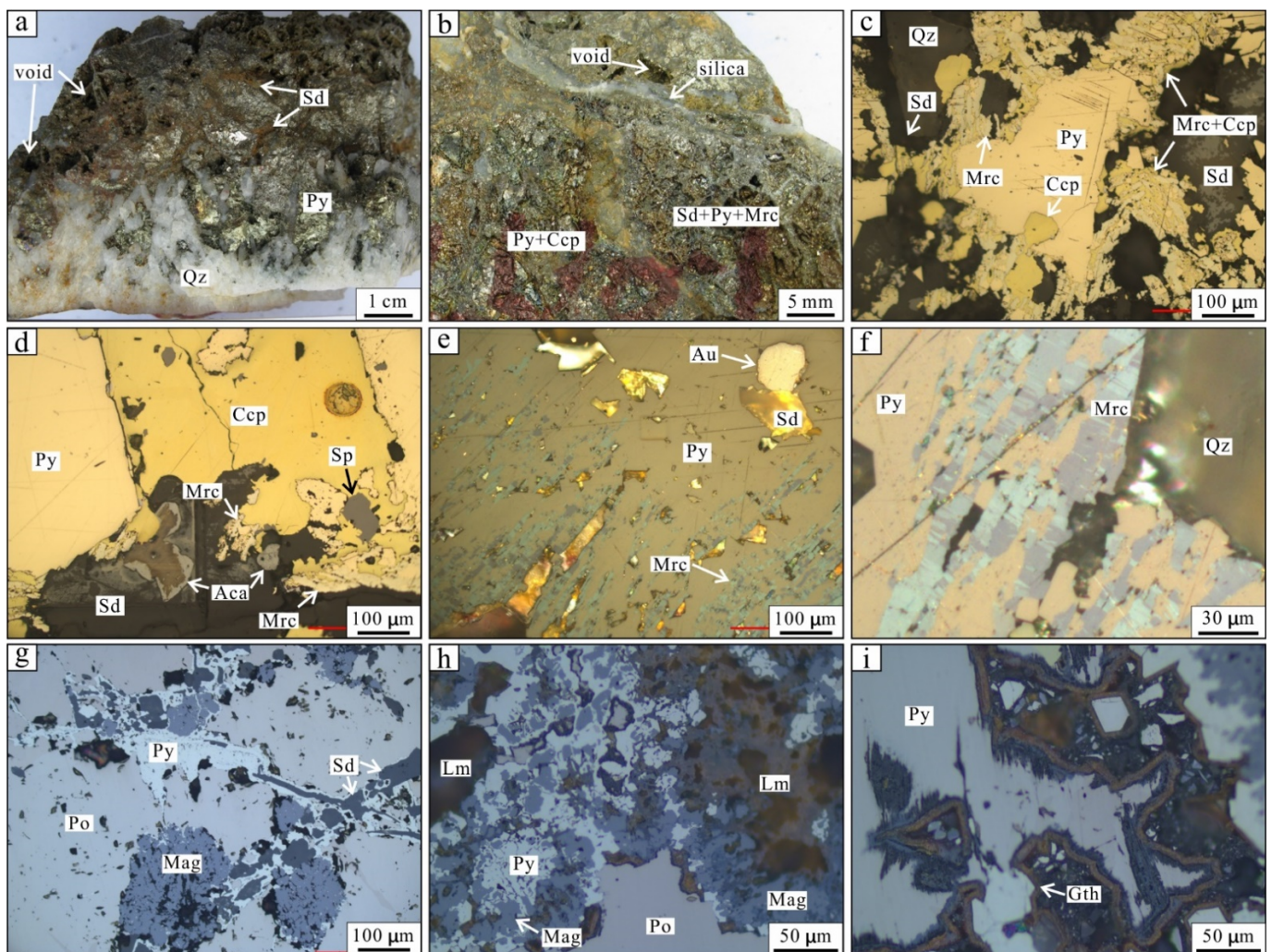


Figure 3. Hand samples from the supergene enrichment zone of the Linglong gold deposit (a,b) and their photomicrographs under reflected light (c–i). The ores are vuggy (a) and contain the primary pyrite-chalcopyrite-pyrrhotite and the secondary marcasite-acanthite and siderite (c–f) and magnetite-limonite-goethite (g–i) assemblages that are commonly cemented by silica colloids (b). Marcasite grains are usually tabular and are recognizable by their polysynthetic twinning and pleochroism (blue and brownish gray) under crossed polarized reflected light (e,f). Aca: acanthite; Au: visible gold grain; Ccp: chalcopyrite; Gth: goethite; Lm: limonite; Mag: magnetite; Mrc: marcasite; Po: pyrrhotite; Py: pyrite; Qz: quartz; Sd: siderite; Sp: sphalerite.

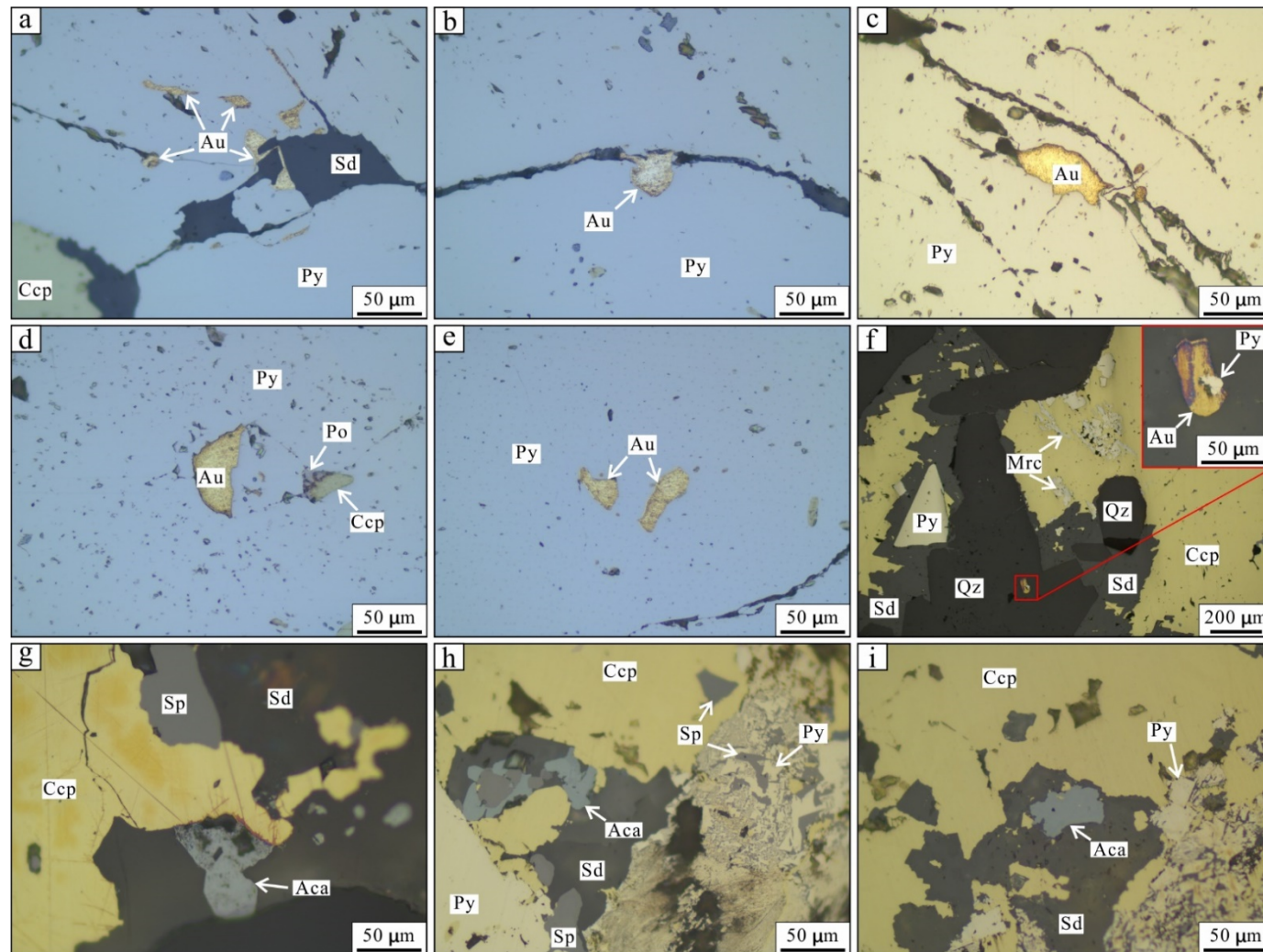


Figure 4. Photomicrographs of gold (a–f) and acanthite (g–i) grains. (a–c) Gold grains in the fractures of pyrite. (d,e) Gold grains as inclusions within pyrite. (f) Gold grain as inclusion within quartz. (g–i) Acanthite grains showing irregular shapes. Abbreviations are the same as those in Figure 3.

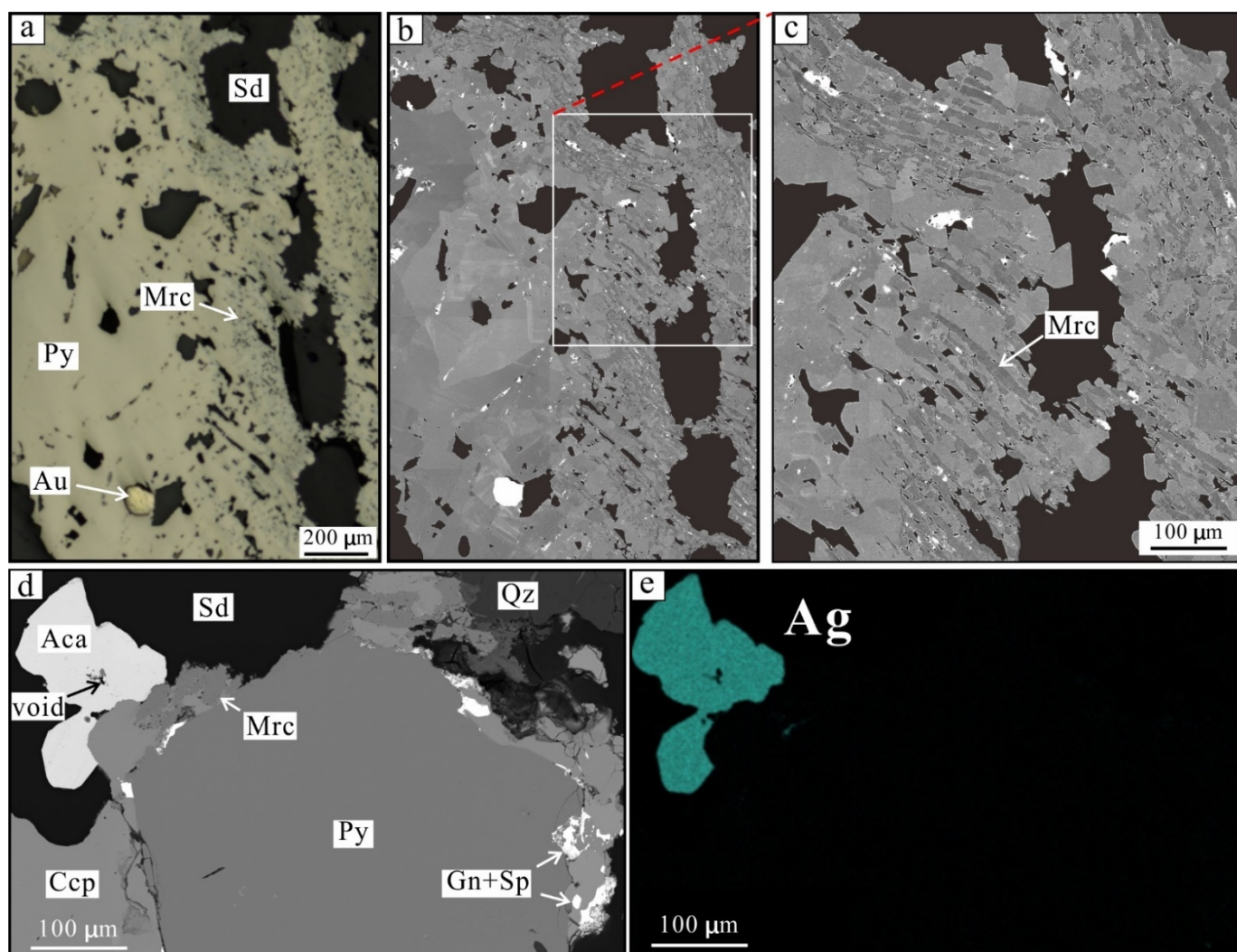


Figure 5. (a) Reflected-light photograph showing the relationships among pyrite, marcasite, and gold. (b) The corresponding SEM-BSE image of (a). (c) SEM-BSE image showing that the marcasite grains display slightly weaker BSE intensity than those of pyrite. Marcasite grains are characterized by thin strips and directional arrangement. (d) SEM-BSE image of the primary assemblages of pyrite and chalcopyrite and the secondary assemblages of acanthite, marcasite, and siderite, with minor galena and sphalerite. (e) EDS map showing the distribution of Ag. Abbreviations are the same as those in Figure 3. Gn: galena; Ag: silver.

4.2. Trace Elemental Compositions of Pyrite and Marcasite

Twenty-three spots on primary pyrite (zoned and homogeneous) and ninety spots on secondary marcasite were analyzed by LA-ICP-MS. The LA-ICP-MS signals of trace elements such as Au, Ag, As, Bi, Sb, Cu, Zn, and Pb are commonly smooth with weak intensities in the pyrite (Figure 6a), indicating their low and relatively stable concentrations. By contrast, the signals are much higher or spiked in the marcasite, suggesting the higher concentrations or the presence of mineral inclusions (Figure 6b,c). The concentrations of Ag, As, Au, Bi, Cu, Pb, Sb, and Zn are several orders of magnitude higher in the marcasite than in the pyrite (Figures 7 and 8). There is no significant difference between the concentrations of trace elements of the zoned and homogeneous pyrite. Specifically, the concentrations of Ag, Au, As, Pb, and Sb are 0.022–4.14 ppm (mean of 0.897 ppm), 0.004–0.029 ppm (mean of 0.011 ppm), 0.011–1.78 ppm (mean of 0.241 ppm), 0.017–7.62 ppm (mean of 2.05 ppm), and 0.001–0.352 ppm (mean of 0.09 ppm), respectively, in the pyrite, whereas in the marcasite, the Ag, Au, As, Pb, and Sb show concentrations of 81.7–6021 ppm (mean of 1111 ppm),

0.003–23.5 ppm (mean of 1.33 ppm), 0.163–1210 ppm (mean of 199 ppm), 2.48–12695 ppm (mean of 789 ppm), and 0.481–3192 ppm (mean of 323 ppm), respectively. The concentrations of the other metals in the two minerals are given in Supplementary Table S1.

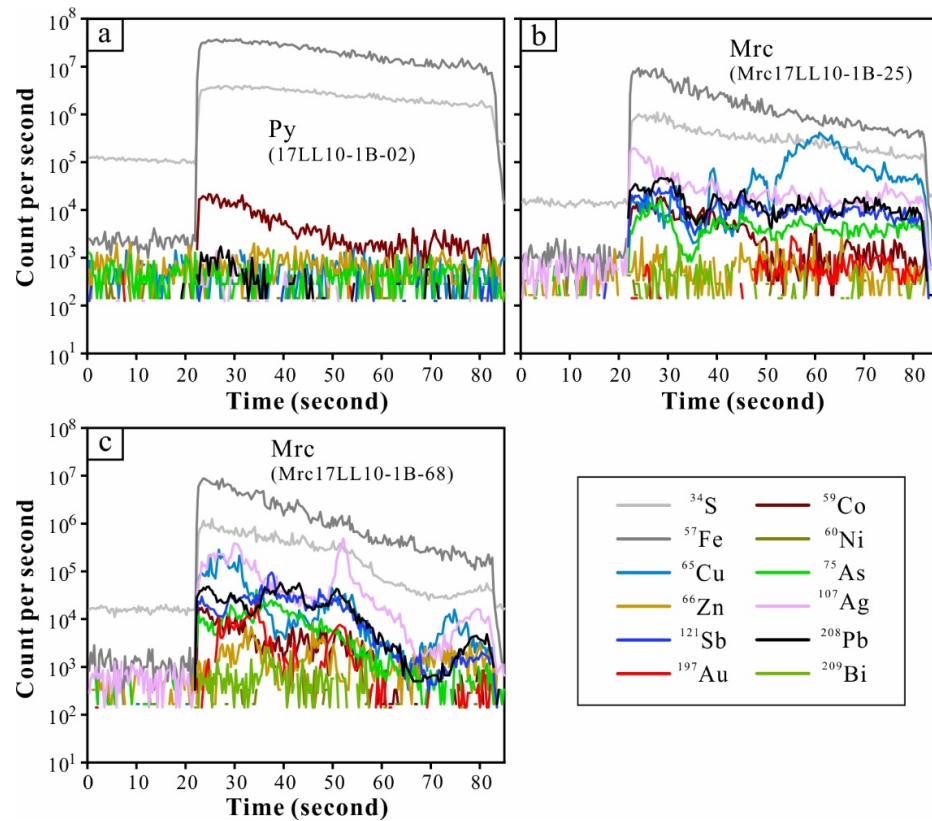


Figure 6. The LA-ICP-MS signals of selected elements in pyrite (a) and marcasite (b,c).

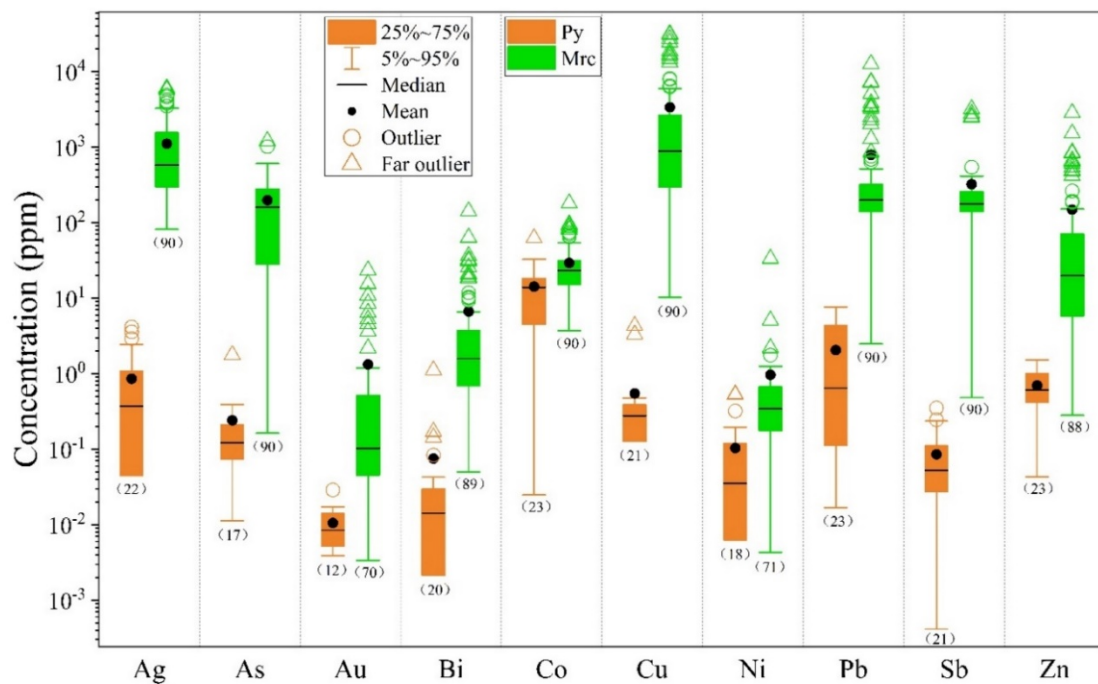


Figure 7. Box plots of selected trace elements in pyrite and marcasite. The number of reliable spots is given in parenthesis.

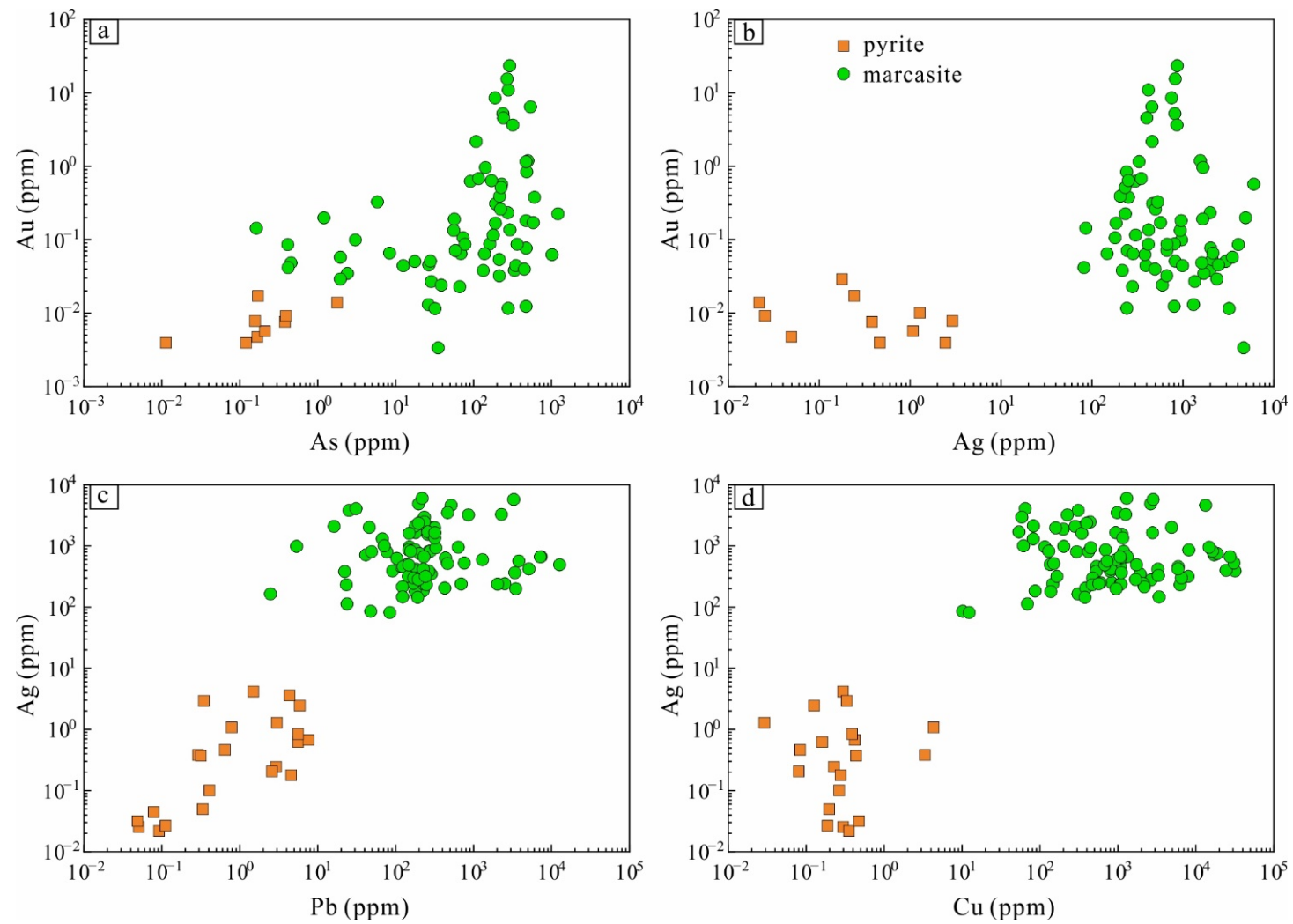


Figure 8. Binary plots of Au vs. As (a), Au vs. Ag (b), Ag vs. Pb (c), and Ag vs. Cu (d) in pyrite and marcasite.

4.3. Elemental Distributions in Pyrite and Marcasite

Elemental mapping by LA-ICP-MS was performed on the representative areas containing both the primary pyrite and secondary marcasite. The results show that As, Au, Ag, Cu, Pb, and Sb are much richer in the marcasite, whereas Co does not show a significant difference between the two minerals. Both the pyrite and marcasite have high Co concentrations. It is noted that Au shows a consistent distribution with that of As, while Ag shows similar distribution to that of Cu and Pb (Figure 9).

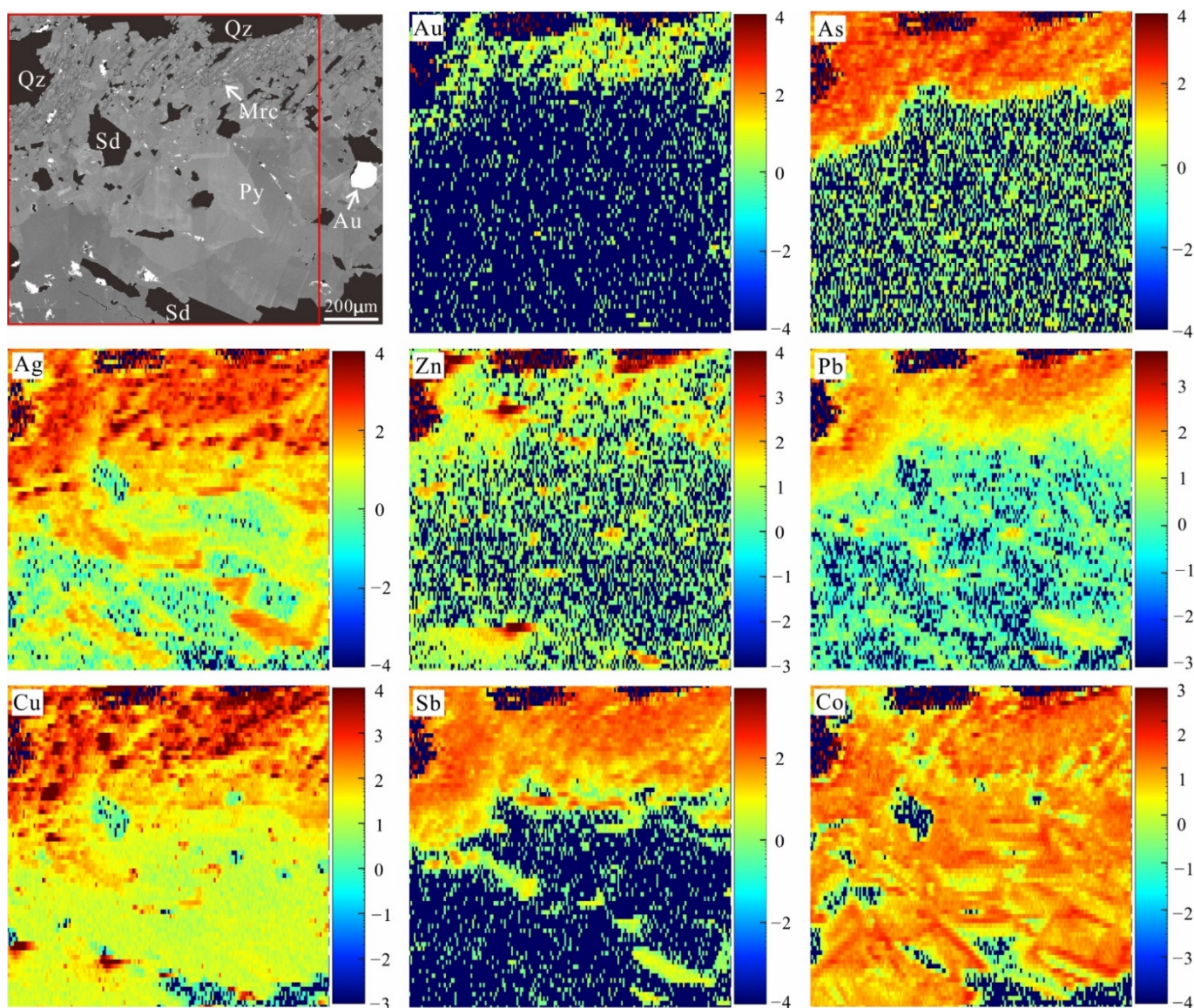


Figure 9. BSE image of pyrite and marcasite and the distributions of selected trace elements obtained by LA-ICP-MS. The semi-quantitative concentrations of the elements were logarithmized.

5. Discussion

5.1. Supergene Processes and the Physicochemical Conditions

Although the supergene profile of the Linglong gold deposit has not been well preserved due to the many years of open-pit and underground mining, the secondary oxide assemblage of magnetite-limonite-goethite in the studied samples (Figure 3g–i) indicates that supergene processes occurred [17,18]. In addition, marcasite and acanthite, which are the common minerals of the supergene zone [9,36,37], do not occur in the primary ore veins

of the Linglong gold deposit [15,16], but are well developed in the studied samples. The primary mineral assemblage of pyrite-chalcopyrite-pyrrhotite, combined with the secondary minerals of marcasite-acanthite and minor magnetite-limonite-goethite, indicate that the studied samples represent the products of the supergene processes in the enrichment zone rather than the leached cap or the oxidized zone.

Marcasite has the same chemical formula as that of pyrite but shows a different crystal structure. It has been found that the marcasite is commonly formed under low-temperature conditions with relatively strong acidity ($\text{pH} < 5$) [38]. The extensive replacement of pyrite by marcasite in this study (Figure 3) thus implies that the replacement occurred in a low-temperature acidic environment. Argentite (Ag_2S) commonly has two allotropic forms [39,40], of which the monoclinic phase $\alpha\text{Ag}_2\text{S}$ (acanthite) occurs at temperatures below 177°C , whereas the isometric phase $\beta\text{Ag}_2\text{S}$ (argentite) occurs at higher temperatures of $179\text{--}586^\circ\text{C}$. When the temperature drops below 177°C , the latter will convert from an isometric to a monoclinic phase but remain unchanged in external appearance (cubic) [39,40]. The Ag_2S crystals in this study show irregular rather than cubic shapes (Figures 4g–i and 5d), combined with the occurrence of marcasite, indicating that they are acanthite formed under low-temperature conditions. Because there was no argentite or acanthite found in the primary quartz–sulfide veins in the Linglong gold deposit [15,16], the acanthite was likely newly formed during the supergene modification. Siderite fills in the fractures of pyrite (both primary and secondary), pyrrhotite, and magnetite (Figure 3) or encloses the acanthite (Figure 4g–i), so that it should form after the formation of the marcasite, magnetite, and acanthite. The forming conditions of siderite are reductive and near neutral, thereby indicating the fluids had evolved to being reductive and near neutral [8,41,42].

Based on the above results, the secondary mineral assemblages changing from magnetite-limonite-goethite to marcasite-acanthite, and to siderite in the studied samples suggest that the associated fluids (groundwater) evolved from being oxidative and weakly acidic in the near-surface zone to reductive and near neutral in the supergene enrichment zone during descending.

5.2. Occurrences of Au and Ag

Gold and silver can occur as nano- to micro-scale particles or as a solid solution in the lattice of the host minerals [43–47]. Visible gold grains (mainly electrum) hosted by pyrite are dominant in the primary ores of the Linglong gold deposit (Figure 4a–f) and also in the other Jiaodong gold deposits [14,48–50]. However, such gold grains were not found in the secondary minerals from the studied samples, suggesting that Au and Ag present in other forms.

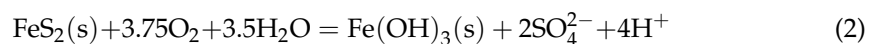
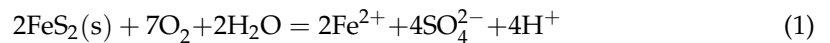
The occurrence of Au and Ag in minerals can be inferred from the time-resolved LA–ICP–MS signals [51,52]. In the studied samples, the smooth and low LA–ICP–MS signals of Au and Ag in the pyrite (Figure 6a) suggest that nanoparticles of Au and Ag are absent. Nonetheless, low concentrations of Au ($0.004\text{--}0.029$ ppm) and Ag ($0.022\text{--}4.14$ ppm) can be detected by LA–ICP–MS, indicating that minor lattice-bound Au and Ag occur in the pyrite. Based on the element-distribution mapping, the Ag shows a similar distribution to that of Cu and Pb (Figure 9), indicating that a certain amount of Ag is associated with the base metal sulfides (e.g., chalcopyrite, galena, and sphalerite). These base metal sulfides have been widely identified in the primary ores of the Linglong gold deposit.

The consistently high LA–ICP–MS signals of Au and Ag in the marcasite (Figure 6b) indicate that lattice-bound Au and Ag occur, which account for the Au and Ag concentrations up to 23.5 ppm and 6021 ppm, respectively. There are also some coupled spikes of Au and Ag signals in some spots (Figure 6c). Combined with no other metals showing consistent spikes with Au and Ag and no visible gold grains found in the marcasite, it is inferred that nanoparticles of Au–Ag alloys occur in the marcasite. In general, the analyzed marcasite grains contain high lattice-bound Au and Ag and a certain amount of nanoparticles of

Au–Ag alloys. It is noteworthy that acanthite (Ag_2S) is widely developed in the studied samples, which should host a large amount of Ag in the supergene enrichment zone.

5.3. Metal Remobilization during Supergene Processes

Supergene processes include the dissolution of parent rock materials, the transportation of soluble elements, and the precipitation of secondary minerals [9,12]. They are mainly controlled by the rock and mineral compositions and the properties of the descending groundwater [11]. As discussed above, the descending groundwater was oxidative and weakly acidic in the near-surface zone, which could dissolve the primary pyrite by oxidation reactions [7,11]. Thus, the pyrite oxidation can be described by Equations (1) and (2) [7,53,54]:



The oxidation of primary pyrite can yield an intermediate thiosulphate ion via Equation (3), which could form complexes with metals [7,8,55]. The Au released from the dissolution of pyrite or Au–Ag alloys can be mobilized as thiosulphate complexes (Figure 10). These processes are described by the combination of Equations (3) and (4):

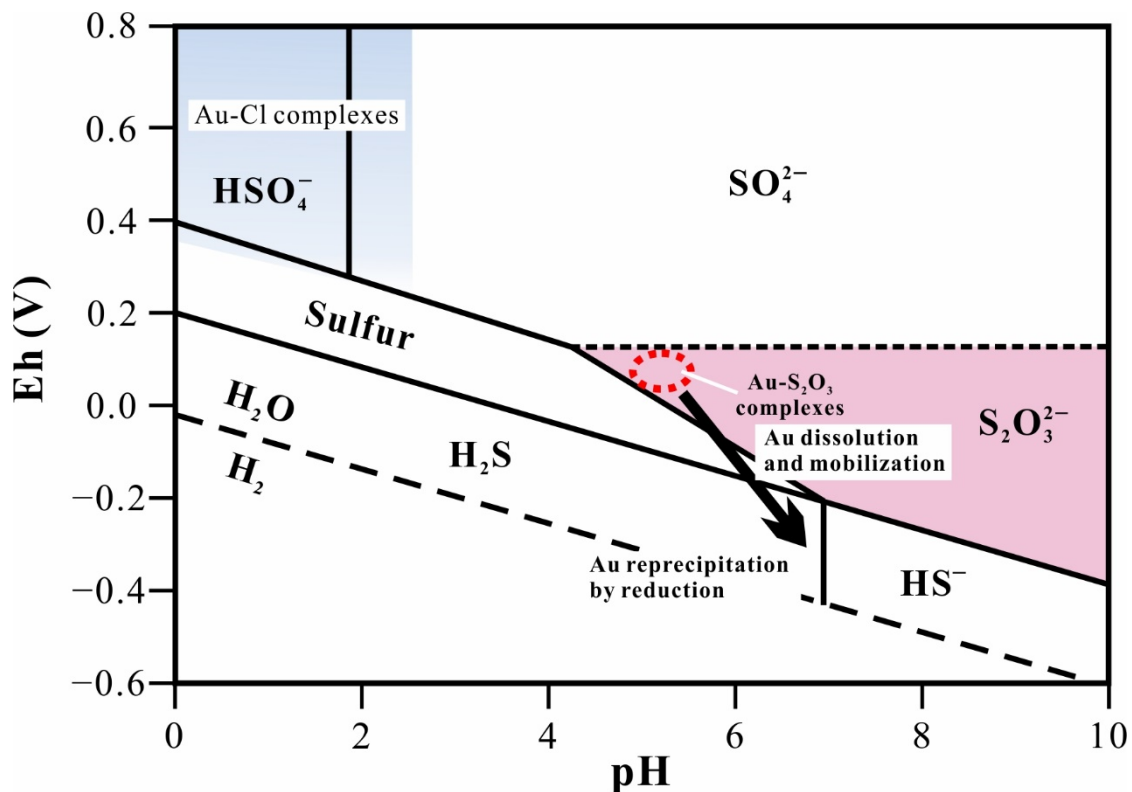
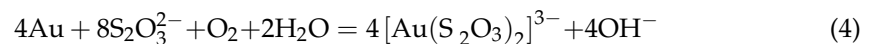
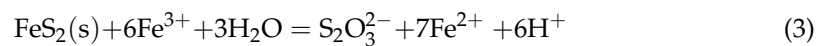


Figure 10. Schematic pH–Eh diagram for 5×10^{-3} molar dissolved sulfur at 25°C (reproduced from Craw et al. [8] with permission of Taylor & Francis Ltd.). Metastable thiosulphate ions are produced from the oxidation of primary pyrite under weakly acidic conditions (red dashed domain). Gold is transported as thiosulphate complexes in the oxidation zone and precipitated in the supergene enrichment zone by reduction (black arrow). In contrast, gold chloride complexes are stable only in the low-pH, high-Eh, and Cl-rich conditions (top left gray area).

Gold can also be transported as chloride complexes in solutions [56], which, however, is ruled out in this study because gold chloride complexes mainly occur in low-pH, high-Eh, and Cl-rich environments (Figure 10) [7,8]. For Ag, under the acidic and oxidized conditions, it has stronger mobility than that of gold [57] and can also be transported as thiosulphate complexes [7,8].

The Au- and Ag-thiosulphate complexes were transported downward. Either reduction or further oxidation and the change in pH condition can destabilize the thiosulphate complexes (Figure 10) [8,57–59]. In this study, the weakly acidic and oxidative groundwater evolved into a near neutral and reductive fluid at deeper depth due to the buffering of pyrrhotite-bearing ore rocks. As a result, the thiosulphate was reduced to H₂S or HS[−] (Figure 10), leading to the destabilization of the Au and Ag thiosulphate complexes and thus the deposition of Au and Ag.

5.4. Implications

In the supergene enrichment zone of the studied deposit, almost all gold grains are found in the fractures or as inclusions within the primary pyrite (Figure 4a–f), indicating they formed under hypogene processes rather than supergene processes and did not dissolve. Rare lattice-bound Au (0.004–0.029 ppm, mean of 0.011 ppm) and Ag (0.022–4.14 ppm, mean of 0.897 ppm) were found in the primary pyrite. In contrast, the marcasite grains generated through supergene processes show one to three orders of magnitude higher lattice-bound Au (0.003–23.5 ppm, mean of 1.33 ppm) and Ag (81.7–6021 ppm, mean of 1111 ppm) concentrations, but contain no visible gold. This indicates that the supergene processes significantly mobilized Au and Ag from the primary minerals to the secondary minerals through dissolution–reprecipitation. Marcasite is orthorhombic, whereas pyrite is isometric [60]. The former is more imperfect in crystal structure and thus prone to having more lattice or structural defects. This would facilitate the incorporation of metals into the marcasite. In addition, the low-temperature, reductive conditions enhanced the coupled incorporation of As and Au into marcasite [43,61]. Since previous studies mainly focused on the visible electrum grains in the primary ores, the enrichment of Au and Ag in the marcasite suggests that it is also possible to utilize the lattice-bound Au and Ag. In addition, the newly formed Ag–S mineral (acanthite) in the supergene enrichment zone indicates that fractionation between the Au and Ag occurred. This led to the further enrichment of Ag, which can facilitate the extraction of Ag.

6. Conclusions

The near-surface ores of the Linglong gold deposit have undergone supergene modification, resulting in the formation of a supergene enrichment zone. Secondary mineral assemblages were formed after the primary pyrite, pyrrhotite and chalcopyrite and changed from magnetite-limonite-goethite, to marcasite-acanthite, and to siderite. These mineral assemblages and variations suggest that the associated fluids (groundwater) evolved from being oxidative and weakly acidic in the near-surface zone to reductive and near neutral in the supergene enrichment zone. Gold and Ag were released from the primary Au- and Ag-bearing minerals (mainly electrum and pyrite) dissolved by the oxidative groundwater and transported as thiosulphate complexes downward. These complexes precipitated in the supergene enrichment zone due to the decreasing Eh, forming the Au- and Ag-rich sulfides (mainly marcasite and acanthite). The supergene processes not only led to the remarkable mobilization of Au and Ag, but also the fractionation between them. More attention needs to be paid to the supergene enrichment zones because they can become favorable targets for mining and utilization.

Supplementary Materials: The following are available online at <https://www.mdpi.com/article/10.3390/min12030367/s1>, Table S1: LA-ICP-MS elemental compositions of pyrite and marcasite from the supergene enrichment zone of the Linglong gold deposit.

Author Contributions: Conceptualization, H.W. and T.L.; methodology, H.W., T.L. and H.H.; validation, T.L.; investigation, H.W., T.L., Y.C. and L.S.; resources, H.W., T.L., Y.C. and L.S.; data curation, T.L.; writing—original draft preparation, H.W.; writing—review and editing, T.L.; funding acquisition, T.L. All authors have read and agreed to the published version of the manuscript.

Funding: This research was funded by the National Key Research and Development Programs of China (Grant Number 2018YFA0702603) and the National Natural Science Foundation of China (Grant Number 41873048).

Acknowledgments: We are grateful to Shaohua Dong and Zhihui Dai for their kind support in the SEM and LA-ICP-MS analyses, respectively. We would like to thank the reviewers, the academic and assistant editors for helping us to improve the manuscript.

Conflicts of Interest: The authors declare no conflict of interest.

References

1. Hastie, E.C.G.; Schindler, M.; Kontak, D.J.; Lafrance, B. Transport and coarsening of gold nanoparticles in an orogenic deposit by dissolution–reprecipitation and Ostwald ripening. *Commun. Earth Environ.* **2021**, *2*, 57. [[CrossRef](#)]
2. Hastie, E.C.G.; Kontak, D.J.; Lafrance, B. Gold Remobilization: Insights from Gold Deposits in the Archean Swayze Greenstone Belt, Abitibi Subprovince, Canada. *Econ. Geol.* **2020**, *115*, 241–277. [[CrossRef](#)]
3. Petrella, L.; Thébaud, N.; Evans, K.; LaFlamme, C.; Occhipinti, S. The role of competitive fluid–rock interaction processes in the formation of high-grade gold deposits. *Geochim. Cosmochim. Acta* **2021**, *313*, 38–54. [[CrossRef](#)]
4. Saunders, J.A.; Burke, M.; Brueseke, M.E. Scanning-electron-microscope imaging of gold (electrum) nanoparticles in middle Miocene bonanza epithermal ores from northern Nevada, USA. *Miner. Depos.* **2020**, *55*, 389–398. [[CrossRef](#)]
5. Saunders, J.A.; Burke, M. Formation and Aggregation of Gold (Electrum) Nanoparticles in Epithermal Ores. *Minerals* **2017**, *7*, 163. [[CrossRef](#)]
6. Ramzey, M.; Abd El-Rahman, Y.; Said, A. Weathering products at the historic Qulaan gold prospect, Eastern Desert, Egypt: Implication on the mobility and distribution of arsenic, gold and silver. *Jafes* **2021**, *182*, 104276. [[CrossRef](#)]
7. Dunn, S.C.; von der Heyden, B.P. Gold remobilization in gossans of the Amani area, southwestern Tanzania. *Ore Geol. Rev.* **2021**, *131*, 104033. [[CrossRef](#)]
8. Craw, D.; MacKenzie, D.; Grieve, P. Supergene gold mobility in orogenic gold deposits, Otago Schist, New Zealand. *N. Z. J. Geol. Geophys.* **2015**, *58*, 123–136. [[CrossRef](#)]
9. Yesares, L.; Sáez, R.; Nieto, J.M.; de Almodóvar, G.R.; Cooper, S. Supergene enrichment of precious metals by natural amalgamation in the Las Cruces weathering profile (Iberian Pyrite Belt, SW Spain). *Ore Geol. Rev.* **2014**, *58*, 14–26. [[CrossRef](#)]
10. Howell, R.J. Supergene gold mineralogy at Ashanti, Ghana: Implications for the supergene behaviour of gold. *Miner. Mag.* **1992**, *56*, 545–560. [[CrossRef](#)]
11. Reich, M. Supergene. In *Encyclopedia of Geochemistry: A Comprehensive Reference Source on the Chemistry of the Earth*; White, W.M., Ed.; Springer International Publishing: Cham, Switzerland, 2016; pp. 1–2.
12. Reich, M.; Vasconcelos, P.M. Geological and economic significance of supergene metal deposits. *Elements* **2015**, *11*, 305–310. [[CrossRef](#)]
13. Andreu, E.; Torro, L.; Proenza, J.A.; Domenech, C.; Garcia-Casco, A.; Villanova de Benavent, C.; Chavez, C.; Espallat, J.; Lewis, J.F. Weathering profile of the Cerro de Maimon VMS deposit (Dominican Republic): Textures, mineralogy, gossan evolution and mobility of gold and silver. *Ore Geol. Rev.* **2015**, *65*, 165–179. [[CrossRef](#)]
14. Deng, J.; Yang, L.; Groves, D.I.; Zhang, L.; Qiu, K.; Wang, Q. An integrated mineral system model for the gold deposits of the giant Jiaodong province, eastern China. *Earth Sci. Rev.* **2020**, *208*, 103274. [[CrossRef](#)]
15. Guo, L.; Goldfarb, R.J.; Wang, Z.; Li, R.; Chen, B.; Li, J. A comparison of Jiaojia- and Linglong-type gold deposit ore-forming fluids: Do they differ? *Ore Geol. Rev.* **2017**, *88*, 511–533. [[CrossRef](#)]
16. Wen, B.; Fan, H.; Santosh, M.; Hu, F.; Pirajno, F.; Yang, K. Genesis of two different types of gold mineralization in the Linglong gold field, China: Constrains from geology, fluid inclusions and stable isotope. *Ore Geol. Rev.* **2015**, *65*, 643–658. [[CrossRef](#)]
17. Wang, J.; Zhang, X. Oxidation-leaching loss, secondary enrichment and the determination of indicative evaluation index for gold deposits. *Geol. Explor.* **1991**, *27*, 13–18. (In Chinese with English Abstract)
18. Wang, J.; Feng, W. The Linglong gold ore deposit and the metallogenic model. *Contrib. Geol. Miner. Resour. Res.* **1991**, *6*, 18–35. (In Chinese with English Abstract)
19. Zhai, M.; Santosh, M. Metallogeny of the North China Craton: Link with secular changes in the evolving Earth. *Gondwana Res.* **2013**, *24*, 275–297. [[CrossRef](#)]
20. Jahn, B.M.; Liu, D.; Wan, Y.; Song, B.; Wu, J. Archean crustal evolution of the Jiaodong Peninsula, China, as revealed by zircon SHRIMP geochronology, elemental and Nd-isotope geochemistry. *Am. J. Sci.* **2008**, *308*, 232–269. [[CrossRef](#)]
21. Wan, Y.; Song, B.; Liu, D.; Wilde, S.A.; Wu, J.; Shi, Y.; Yin, X.; Zhou, H. SHRIMP U–Pb zircon geochronology of Palaeoproterozoic metasedimentary rocks in the North China Craton: Evidence for a major Late Palaeoproterozoic tectonothermal event. *Precamb. Res.* **2006**, *149*, 249–271. [[CrossRef](#)]

22. Li, X.; Fan, H.; Hu, F.; Hollings, P.; Yang, K.; Liu, X. Linking lithospheric thinning and magmatic evolution of late Jurassic to early cretaceous granitoids in the Jiaobei Terrane, southeastern North China Craton. *Lithos* **2019**, *324*, 280–296. [[CrossRef](#)]
23. Yang, K.; Fan, H.; Santosh, M.; Hu, F.; Wilde, S.A.; Lan, T.; Lu, L.; Liu, Y. Reactivation of the Archean lower crust: Implications for zircon geochronology, elemental and Sr-Nd-Hf isotopic geochemistry of late Mesozoic granitoids from northwestern Jiaodong Terrane, the North China Craton. *Lithos* **2012**, *146*, 112–127. [[CrossRef](#)]
24. Lan, T.; Fan, H.-R.; Santosh, M.; Hu, F.; Yang, K.; Yang, Y.; Liu, Y. Geochemistry and Sr-Nd-Pb-Hf isotopes of the Mesozoic Dadian alkaline intrusive complex in the Sulu orogenic belt, eastern China: Implications for crust-mantle interaction. *Chem. Geol.* **2011**, *285*, 97–114. [[CrossRef](#)]
25. Goss, S.C.; Wilde, S.A.; Wu, F.; Yang, J. The age, isotopic signature and significance of the youngest Mesozoic granitoids in the Jiaodong Terrane, Shandong Province, North China Craton. *Lithos* **2010**, *120*, 309–326. [[CrossRef](#)]
26. Deng, J.; Liu, X.; Wang, Q.; Dilek, Y.; Liang, Y. Isotopic characterization and petrogenetic modeling of Early Cretaceous mafic diiking-Lithospheric extension in the North China craton, eastern Asia. *Geol. Soc. Am. Bull.* **2017**, *129*, 1379–1407. [[CrossRef](#)]
27. Zhang, L.; Weinberg, R.F.; Yang, L.; Groves, D.I.; Sai, S.; Matchan, E.; Phillips, D.; Kohn, B.P.; Miggins, D.P.; Liu, Y.; et al. Mesozoic Orogenic Gold Mineralization in the Jiaodong Peninsula, China: A Focused Event at 120 ± 2 Ma During Cooling of Pregold Granite Intrusions. *Econ. Geol.* **2020**, *115*, 415–441. [[CrossRef](#)]
28. Song, M.; Li, S.; Santosh, M.; Zhao, S.; Yu, S.; Yi, P.; Cui, S.; Lv, G.; Xu, J.; Song, Y.; et al. Types, characteristics and metallogensis of gold deposits in the Jiaodong Peninsula, Eastern North China Craton. *Ore Geol. Rev.* **2015**, *65*, 612–625. [[CrossRef](#)]
29. Li, L.; Santosh, M.; Li, S.-R. The ‘Jiaodong type’ gold deposits: Characteristics, origin and prospecting. *Ore Geol. Rev.* **2015**, *65*, 589–611. [[CrossRef](#)]
30. Qiu, Y.M.; Groves, D.I.; McNaughton, N.J.; Wang, L.G.; Zhou, T.H. Nature, age, and tectonic setting of granitoid-hosted, orogenic gold deposits of the Jiaodong Peninsula, eastern North China craton, China. *Miner. Depos.* **2002**, *37*, 283–305. [[CrossRef](#)]
31. Shen, J.; Li, S.; Ma, G.; Liu, Y.; YU, H.; Liu, H. Typomorphic characteristics of pyrite from the Linglong gold deposit: Its vertical variation and prospecting significance. *Earth Sci. Front.* **2013**, *20*, 55–75. (In Chinese with English Abstract)
32. Wen, B.; Fan, H.; Hu, F.; Liu, X.; Yang, K.; Sun, Z.; Sun, Z. Fluid evolution and ore genesis of the giant Sanshandao gold deposit, Jiaodong gold province, China: Constrains from geology, fluid inclusions and H-O-S-He-Ar isotopic compositions. *J. Geochem. Explor.* **2016**, *171*, 96–112. [[CrossRef](#)]
33. Wilson, S.A.; Ridley, W.I.; Koenig, A.E. Development of sulfide calibration standards for the laser ablation inductively-coupled plasma mass spectrometry technique. *J. Anal. At. Spectrom.* **2002**, *17*, 406–409. [[CrossRef](#)]
34. Danyushevsky, L.; Robinson, P.; Gilbert, S.; Norman, M.; Large, R.; McGoldrick, P.; Shelley, M. Routine quantitative multi-element analysis of sulphide minerals by laser ablation ICP-MS: Standard development and consideration of matrix effects. *Geochem. Explor. Environ. Anal.* **2011**, *11*, 51–60. [[CrossRef](#)]
35. Paton, C.; Hellstrom, J.; Paul, B.; Woodhead, J.; Hergt, J. Iolite: Freeware for the visualisation and processing of mass spectrometric data. *J. Anal. At. Spectrom.* **2011**, *26*, 2508–2518. [[CrossRef](#)]
36. Martycák, K.; Zeman, J.; Vacek-Veselý, M. Supergene processes on ore deposits—A source of heavy metals. *Environ. Geol.* **1994**, *23*, 156–165. [[CrossRef](#)]
37. Clough, D.M.; Craw, D. Authigenic gold-marcasite association; evidence for nugget growth by chemical accretion in fluvial gravels, Southland, New Zealand. *Econ. Geol.* **1989**, *84*, 953–958. [[CrossRef](#)]
38. Murowchick, J.B.; Barnes, H.L. Marcasite precipitation from hydrothermal solutions. *Geochim. Cosmochim. Acta* **1986**, *50*, 2615–2629. [[CrossRef](#)]
39. Sadovnikov, S.; Gusev, A.; Rempel, A. An in situ high-temperature scanning electron microscopy study of acanthite–argentite phase transformation in nanocrystalline silver sulfide powder. *Phys. Chem. Chem. Phys.* **2015**, *17*, 20495–20501. [[CrossRef](#)]
40. Sharma, R.C.; Chang, Y.A. The Ag–S (Silver–Sulfur) system. *Bull. Alloy Phase Diag.* **1986**, *7*, 263–269. [[CrossRef](#)]
41. Mozley, P.S.; Wersin, P. Isotopic composition of siderite as an indicator of depositional environment. *Geology* **1992**, *20*, 817–820. [[CrossRef](#)]
42. Craw, D. Water–rock interaction and acid neutralization in a large schist debris dam, Otago, New Zealand. *Chem. Geol.* **2000**, *171*, 17–32. [[CrossRef](#)]
43. Pokrovski, G.S.; Escoda, C.; Blanchard, M.; Testemale, D.; Hazemann, J.L.; Gouy, S.; Kokh, M.A.; Boiron, M.C.; de Parseval, F.; Aigouy, T.; et al. An arsenic-driven pump for invisible gold in hydrothermal systems. *Geochem. Perspect. Lett.* **2021**, *17*, 39–44. [[CrossRef](#)]
44. Liang, Q.; Xie, Z.; Song, X.; Wirth, R.; Xia, Y.; Cline, J. Evolution of invisible Au in arsenian pyrite in Carlin-type Au deposits. *Econ. Geol.* **2021**, *116*, 515–526. [[CrossRef](#)]
45. Tauson, V.L.; Kravtsova, R.G.; Smagunov, N.V.; Spiridonov, A.M.; Grebenshchikova, V.I.; Budyak, A.E. Structurally and superficially bound gold in pyrite from deposits of different genetic types. *Russ. Geol. Geophys.* **2014**, *55*, 273–289. [[CrossRef](#)]
46. Cook, N.J.; Ciobanu, C.L.; Mao, J. Textural control on gold distribution in As-free pyrite from the Dongping, Huangtuliang and Hougou gold deposits, North China Craton (Hebei Province, China). *Chem. Geol.* **2009**, *264*, 101–121. [[CrossRef](#)]
47. Reich, M.; Kesler, S.E.; Utsunomiya, S.; Palenik, C.S.; Chryssoulis, S.L.; Ewing, R.C. Solubility of gold in arsenian pyrite. *Geochim. Cosmochim. Acta* **2005**, *69*, 2781–2796. [[CrossRef](#)]

48. Yang, L.; Deng, J.; Wang, Z.; Guo, L.; Li, R.; Groves, D.I.; Danyushevsky, L.V.; Zhang, C.; Zheng, X.; Zhao, H. Relationships Between Gold and Pyrite at the Xincheng Gold Deposit, Jiaodong Peninsula, China: Implications for Gold Source and Deposition in a Brittle Epizonal Environment. *Econ. Geol.* **2016**, *111*, 105–126. [[CrossRef](#)]
49. Yuan, Z.; Li, Z.; Li, J.; Zhao, X.; Wu, Y.; Xu, H.; Sun, H. Occurrence and remobilization of gold in the Dayingezhuang deposit in Jiaodong, North China Craton: Evidence from textural and geochemical features of pyrite. *Ore Geol. Rev.* **2021**, *136*, 104243. [[CrossRef](#)]
50. Peng, H.; Fan, H.; Liu, X.; Wen, B.; Zhang, Y.; Feng, K. New insights into the control of visible gold fineness and deposition: A case study of the Sanshandao gold deposit, Jiaodong, China. *Am. Miner.* **2021**, *106*, 135–149. [[CrossRef](#)]
51. Deditius, A.P.; Reich, M.; Kesler, S.E.; Utsunomiya, S.; Chryssoulis, S.L.; Walshe, J.; Ewing, R.C. The coupled geochemistry of Au and As in pyrite from hydrothermal ore deposits. *Geochim. Cosmochim. Acta* **2014**, *140*, 644–670. [[CrossRef](#)]
52. Large, R.R.; Danyushevsky, L.; Hollit, C.; Maslennikov, V.; Meffre, S.; Gilbert, S.; Bull, S.; Scott, R.; Emsbo, P.; Thomas, H.; et al. Gold and Trace Element Zonation in Pyrite Using a Laser Imaging Technique: Implications for the Timing of Gold in Orogenic and Carlin-Style Sediment-Hosted Deposits. *Econ. Geol.* **2009**, *104*, 635–668. [[CrossRef](#)]
53. Nicholson, R.V.; Gillham, R.W.; Reardon, E.J. Pyrite oxidation in carbonate-buffered solution: 1. *Experimental kinetics. Geochim. Cosmochim. Acta* **1988**, *52*, 1077–1085. [[CrossRef](#)]
54. Garrels, R.; Thompson, M. Oxidation of pyrite by iron sulfate solutions. *Am. J. Sci.* **1960**, *258*, 57–67.
55. Grosse, A.C.; Dicoski, G.W.; Shaw, M.J.; Haddad, P.R. Leaching and recovery of gold using ammoniacal thiosulfate leach liquors (a review). *Hydrometallurgy* **2003**, *69*, 1–21. [[CrossRef](#)]
56. Williams-Jones, A.E.; Bowell, R.J.; Migdisov, A.A. Gold in Solution. *Elements* **2009**, *5*, 281–287. [[CrossRef](#)]
57. Webster, J.G. The solubility of gold and silver in the system Au–Ag–S–O₂–H₂O at 25 °C and 1 atm. *Geochim. Cosmochim. Acta* **1986**, *50*, 1837–1845. [[CrossRef](#)]
58. Kerr, G.; Craw, D. Mineralogy and Geochemistry of Biologically-Mediated Gold Mobilisation and Redeposition in a Semiarid Climate, Southern New Zealand. *Minerals* **2017**, *7*, 147. [[CrossRef](#)]
59. Reed, M.H.; Palandri, J. Sulfide Mineral Precipitation from Hydrothermal Fluids. *Rev. Miner. Geochem.* **2006**, *61*, 609–631. [[CrossRef](#)]
60. Hyde, B.; Okeeffe, M. Marcasite and pyrite (FeS₂). *Austral J. Chem.* **1996**, *49*, 867–872. [[CrossRef](#)]
61. Xing, Y.; Brugger, J.; Tomkins, A.; Shvarov, Y. Arsenic evolution as a tool for understanding formation of pyritic gold ores. *Geology* **2019**, *47*, 335–338. [[CrossRef](#)]